Multilayer Laue lenses at high X-ray energies: performance and applications

Murray, Kevin T.; Pedersen, Anders Filsøe; Mohacsi, Istvan; Detlefs, Carsten; Morgan, Andrew J.; Prasciolu, Mauro; Yildirim, Can; Simons, Hugh; Jakobsen, Anders Clemen; Chapman, Henry N.

Total number of authors:
12

Published in:
Optics Express

Link to article, DOI:
10.1364/OE.27.007120

Publication date:
2019

Document Version
Peer reviewed version

Multilayer Laue lenses at high x-ray energies: Performance and applications

KEVIN T. MURRAY,[1] ANDERS F. PEDERSEN,[2] ISTVAN MOHACSI,[1] CARSTEN DETLEFS,[3] ANDREW J. MORGAN,[4] MAURO PRASCIOLU,[1] CAN YILDIRIM,[3,5] HUGH SIMONS, [2] ANDERS C. JAKOBSEN,[2] HENRY N. CHAPMAN,[4,6,7] HENNING F. POULSEN,[2] AND SAŠA BAJT[1,*]

[1] *Photon Science DESY, Notkestrasse 85, 22607 Hamburg, Germany*
[2] *Department of Physics, Technical University of Denmark, 2800 Kgs Lyngby, Denmark*
[3] *European Synchrotron Radiation Facility, 71 Avenue des Martyrs, 3800 Grenoble, France*
[4] *Center for Free-Electron Laser Science, DESY, Notkestrasse 85, 22607 Hamburg, Germany*
[5] *OCAS, J. F. Kennedylaan 3, 9060 Zelzate, Belgium*
[6] *Department of Physics, University of Hamburg, Luruper Chaussee 149, 22607 Hamburg, Germany*
[7] *Centre for Ultrafast Imaging, Luruper Chaussee 149, 22607 Hamburg, Germany*
[*] *sasa.bajt@desy.de*

Abstract: X-ray microscopy at energies above 15 keV is limited by the optics available. Theoretically, wedged multilayer Laue lenses may transform the field as their numerical aperture can be superior to the compound refractive lenses used today. We present experimental results for two pair of lenses designed to work at 17.3 keV with a focal length of ~10 mm and at 34.5 keV with focal length of ~40 mm. The 17.3 keV lens had a numerical aperture of 2.0×10^{-3}, and exhibited a 34×36 nm^2 focal spot in a projection geometry with an efficiency of 51 % $\times$ 54 %. The field-of-view is shown to be constrained by the rocking curve width to be 9.5×15.1 μm^2. The wavefront of the lenses showed a high reproducibility as determined by ptychography and speckle tracking. We demonstrate the applicability of multilayer Laue lenses for high resolution direct imaging. In the bright field mode, phase contrast is enabled via defocusing. As an example for use in the dark field mode, domains in a $BaTiO_3$ single crystal are imaged.

1. Introduction

Hard x-rays with photon energies in the range of 15 keV to 500 keV are used for imaging within a very broad range of applications, covering the fields of energy research [1], materials science [2], biology [3], and many others. Increasing the photon energy enables samples of higher density and thickness to be investigated while reducing correction terms and minimizing dose levels e.g. by utilizing phase contrast or Compton scattering [4]. Furthermore, state-of-the-art instruments operating in this spectral regime permit imaging with sub-micrometer resolution.

In this work, we focus on hard x-ray microscopy methods [5–8](added ref), where an x-ray lens is used as an objective to form a real or virtual source for point-projection (holographic) imaging, and where the lens is used as an image-forming objective [9, 10](added ref). Both projection holography and direct imaging provide full-field images. That is, they do not require scanning of a focused probe. Projection holography is a phase-sensitive bright-field imaging technique whereas direct imaging (forming a real image of the object onto a detector) can be carried out in a bright-field mode (offering absorption contrast) or in a dark-field mode (offering contrast based on scattering) [11](added ref). The latter is a recent technique that enables nondestructive analysis of the structure, orientation and strain of crystallites within large or embedded sampling volumes such as polycrystalline materials [12, 13]. First applications include studies of dislocations [14], plasticity in metals [12] and domain evolution in ferroelectrics [15]. The choice and quality of the lens is important for all modalities of hard x-ray microscopy as it determines the spatial

resolution of images and the speed at which they can be acquired.

High resolution imaging requires a lens able to discern closely-spaced objects, or equivalently able to focus a beam to a small spot. However, such focusing is challenging to achieve with hard x-rays due to their small interaction cross section with matter. The refractive index $\tilde{n}$ can be expressed as $\tilde{n} = 1 - \delta + i\beta$, where for hard x-rays both the refractive index decrement δ and the absorption index β are small ($\ll 10^{-4}$). Optics that can achieve a spatial resolution or spot diameters in the nanometer range [5, 16, 17] can utilize several modes of linear and elastic interactions of x-rays with matter, namely reflection, refraction, or diffraction. Examples of such optical systems are, respectively, Kirkpatrick-Baez mirrors [18], compound refractive lenses [19], and Fresnel zone plates [20].

Kirkpatrick-Baez (KB) mirrors utilize the total external reflection of x-rays at grazing angles from a curved surface [18]. The critical angle of the total external reflection is proportional to $\sqrt{\delta}$ and therefore approximately inversely proportional to the photon energy. Therefore, for energies >20 keV the numerical aperture (NA) of such optics cannot exceed $\sim 10^{-2}$, even for mirrors coated with a material of high atomic number. Adding a multilayer coating to the mirror can increase the grazing angle at which x-rays reflect, and hence can increase the achievable NA. The performance of such mirrors is often limited by the figure error of the mirror surface, which can be improved by active correction towards the theoretical limit. In this way, sub-10 nm focusing at 20 keV has been achieved with a NA of approximately 7×10^{-3} [21]. A 2D focus of 12×13 nm^2 at 33.6 keV was reported recently [7]. However, KB mirrors do not fulfill the Abbe sine condition and can therefore not be used as an objective in full-field microscopy by direct imaging [22].

Another common optical system for focusing hard x-rays is a compound refractive lens (CRL) [19], comprising a stack of individual lenslets, coaxial to the optical axis. If the lenslets are identical, the numerical aperture of a CRL is limited to $\sqrt{2\delta}$. The theoretical resolution limit is approximately 10 nm [23], which corresponds to NA= 4×10^{-3} at 20 keV. However, due to limitations in shaping the lens material [24], the smallest 2D focus reported so far was 47×55 nm^2 at 21 keV with an NA of approximately 0.7×10^{-3} [5]. Recently, using a refractive corrector (the x-ray analogue of a Schmidt corrector), the root mean square phase error of a CRL was decreased from 0.46 π to 0.12 π, with a corresponding improvement in spot size and Strehl ratio [25].

Diffractive optics, such as zone plates (ZPs), consist of diffracting structures that decrease in period with distance from the optical axis. The NA depends on the difference of the deflection angles, which for an axisymmetric lens arises from the smallest period at the ZP boundary. In this case, the NA is exactly equal to the diffraction angle, resulting in a focus size equal to half the outermost zone period, or the size of the smallest linewidth in the ZP. ZPs designed for hard x-rays (>10 keV) need be thick (in the direction parallel to the optical axis) to have reasonable efficiency. To achieve nanometer focusing, lenses must be prepared with zone widths of several nanometers and a thickness of several microns along the beam direction (in the following we refer to this thickness as the depth of the lens). This aspect ratio is beyond what can be fabricated with electron beam lithography [26], a common method for making soft x-ray zone plates. An alternative fabrication method, which can create layered structures with almost no practical limit to the aspect ratio, is based on multilayer deposition [27]. Called multilayer Laue lenses (MLLs), x-ray optics fabricated this way have the potential to produce sub-nanometer spot sizes with high efficiency [28–30]. Point-projection imaging with a spot size of 8.4×6.8 nm^2 and 68 % diffraction efficiency has recently been demonstrated at 16.3 keV [31].

Here we report on the optical performance of MLLs at energies up to 34.5 keV and demonstrate their application for projection imaging, and direct imaging with both bright-field and dark-field illumination. We first briefly describe the design and fabrication of the MLLs (Section 2). In Section 3, the experimental setup (Section 3.1) and the imaging geometries (Section 3.2) used for optics characterization and applications are presented. The results on optical performance

and diffraction efficiency at two different energies (17.3 keV and 34.5 keV) are discussed in Section 4. This includes the analysis of the wavefronts of individual lenses, 2D focus analysis, and presentation of full field microscopy images obtained with these sets of lenses. The final section focuses on full field imaging: the applicability of MLLs is demonstrated with examples of images exhibiting phase and scattering contrast, and the future perspective is briefly outlined.

2. MLL fabrication and operation

MLLs can be prepared by depositing thousands of alternating nanometer thick layers of high- and low-Z material on an atomically smooth substrate [31]. An axisymmetric MLL, which focuses in two dimensions, can be prepared by depositing materials onto a cylindrical wire [32]. MLLs are usually created by deposition onto a flat surface, however, to create a one-dimensional MLL that operates like a cylindrical lens. The multilayers in this work were deposited using magnetron sputtering, but other methods can be used as well [33]. The layer thickness must follow the Fresnel zone plate equation to ensure that the path length from the face of the lens to the focal spot, located at a distance f from the intersection of the face of the lens with the optical axis, increases by $\lambda/2$ for each layer, where λ is the wavelength. For a thin ZP the zone radius r_n of the n^{th} layer obeys $r_n^2 + f^2 = (f + n\lambda/2)^2$ [20, 34]. For a thick zone plate, however, incident collimated rays diffracting from a point at a distance z from the front face of the structure must be deflected such that they achieve a focal length $f - z$. The distance r_n of the n^{th} layer from the optical axis can then be expressed as

$$r_n(z) \approx \underbrace{\sqrt{n\lambda f + \frac{n^2\lambda^2}{4}}}_{\text{ZP condition}} \underbrace{(1 - \frac{z}{2f + n\lambda/2})}_{\text{Bragg's law}} \tag{1}$$

where only the first two terms of a Taylor series of $r_n(z)$ are listed [35](Added ref). We see that the layers decrease in radius r_n with increasing distance z in the direction of the optical axis, meaning that the layers are tilted. This is indeed the condition required by Bragg's law to diffract from a three-dimensional crystal. The angle of the tilt (for focusing of an incident collimated beam) is given by the Bragg angle θ, approximately equal to $r_n/(2f)$ for small angles. This curvature of $2f$ of the layers is equivalent to the imaging condition of a curved spherical mirror at normal incidence (creating a virtual image) or, more aptly, to that of a curved array of reflecting surfaces [36]. Figure 1(a) depicts the structure of a wedged MLL.

Due to the simpler fabrication, MLLs are often designed with parallel (flat) layers. In this case, at least one of the layers can be placed in the reflecting condition by tilting the entire MLL. The number of layers that will efficiently reflect depends on the angular acceptance of the layers – the rocking curve width –which decreases linearly with the layer period d_n. The NA is in this case comparable to previously mentioned x-ray optics and wedging of the layers is thus necessary to achieve NA $> 10^{-3}$. One way to prepare MLLs with the correct $2f$ curvature is to add a mask between the sputtering targets and the substrate during the deposition process Added reference [37–39]. It shadows the surface of the substrate and results in a controlled gradient of the multilayer thickness profile in the penumbra of the mask. It has been demonstrated that by cutting out a slice of a multilayer at a position where the local gradient matches twice the desired focal length, one can obtain the correct wedge to give an efficient MLL in which all layers are in the reflecting condition [31, 38]. To obtain high quality MLLs the multilayer deposition typically starts with the thinnest layers to minimize the impact of accumulation of errors and roughness in the deposition process.

Considering an MLL as a volume grating, such lenses only reflect an incident collimated beam into a transmitted 0^{th} diffraction order, and one diffracting order when the structure is oriented in the reflecting condition. This condition is given by Bragg's law, $\lambda = 2\,d\,sin(\theta)$ (see Fig. 1). For

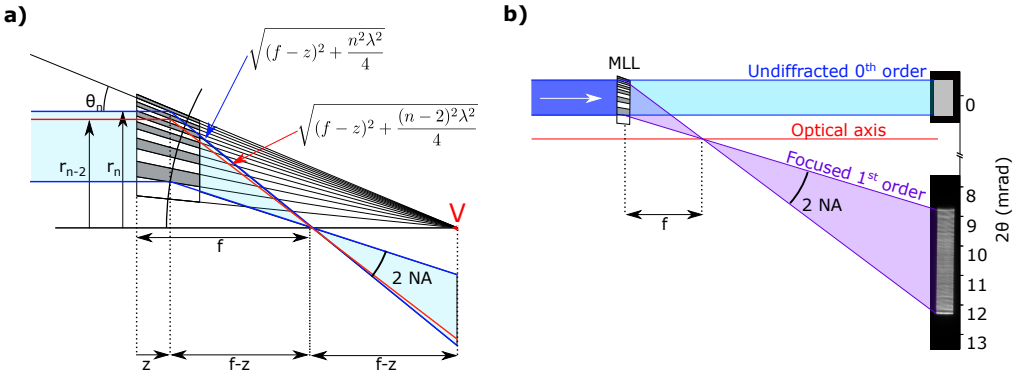

Fig. 1. (a) Schematic of a wedged MLL. Blue lines and the red line depict rays that are diffracted in the lens at a distance z ($z \ll f$) from the entrance surface in the direction of the optical axis. The upper incident blue ray shows the ray diffracted by the nth layer, while the red ray diffracts two layers below it ($n-2$). The optical path lengths of these diffracted rays are provided and the resulting focal length is ($f-z$). The layer boundaries are oriented azimuthally on a circle with radius $2(f-z) \sim 2f$. Hence, each layer simultaneously fulfills the Bragg condition and follows the Fresnel zone plate equation (1). (b) Schematic showing the diffraction orders of a wedged MLL with incident collimated x-rays (darker blue beam). The zero order transmits through the MLL (light blue beam) without change of path. The diffracted first order is a convergent beam, which diverges downstream from the focus (purple beam). The far field intensity of the diffracted order of an example wedged MLL, recorded at 0.13 m distance, is depicted.

the periods and wavelengths considered here, higher diffracting orders (due to spatial frequencies in the structure with periods that are fractions of d) are heavily supressed in wedged MLLs. They can only be observed when tilting the lens, are of extremely low efficiency and only occur over a portion of the lens aperture. (before: cannot be simultaneously excited with the first diffracting order. These only can be observed by tilting the lens [38], and even then, are of extremely low efficiency and only occur over a portion of the lens aperture.) The zero order occurs for all tilts of the structure but its transmission is reduced when light is directed into the diffracting order. In the diffracting condition the fraction of light directed into either the zero order or diffracting order oscillates with the depth of the structure. The efficiency of the diffracting order is optimized at a depth equal to half a Pendellösung period (see Eq. (21) in [30]). As discussed below, efficiencies greater than 80% may be achieved. A negative diffracting order at equal diffraction efficiency occurs when the lens is tilted such that the rays reflect from the opposite side of the layers. For the wedged MLL, this occurs when the lens is oriented such that the vertex of the layers (point V in Fig. 1) is upstream of the lens, in which case the lens creates diverging beam that appears to originate from a point a distance f from the lens.

Only an off-axis portion of a zone plate is usually fabricated, with the thickest (last deposited) layer being some distance from the optical axis. As shown in Fig. 1(b), for the positive (focusing) order, this allows the zero order to be separated from the diffracted order. The zero order and first order beams become separated at a plane between the lens and the focus, where a central beam stop may be placed to prevent off-axis regions of an object to be exposed. In this work, no such central beam stop was needed since the extents of the objects were smaller than the off-axis distance of the lens and the two beams were well separated on the far-field detector.

An MLL fabricated by deposition on a flat substrate (rather than on a cylindrical wire) is an off-axis section of a cylindrical lens, which focuses x-rays only in one direction. Hence, to obtain a 2D focus, a set of two MLLs is required, oriented to focus in orthogonal directions

Table 1. List of MLL design parameters for the lenses used in this paper. Energy, physical aperture size (D - lens dimension), the number of layers (N_{layers}), optical depth, multilayer materials, focal length f, NA, smallest layer period d_{min} and full width half maximum (FWHM) field of views (FOV) are listed. The FOV can be expressed as FOV $\approx f\Delta\theta$, where $\Delta\theta$ is the rocking curve width.

Name	Energy (keV)	f (mm)	D (μm)	N_{layers}	NA (10^{-3})	Optical depth (μm)	Multilayer materials	d_{min} (nm)	FOV (μm)
1h	17.3	9.5	37.2	11350	2	7.0	WC/SiC	7.31	9.5
1v	17.3	13.7	43.5	12778	1.6	6.5	WC/SiC	7.13	15.1
2h	34.5	37	31.6	6612	0.4	8.5	W/SiC	8.47	22.2
2v	34.5	40	55.7	16502	0.7	9.0	WC/SiC	6.01	27.2

(e.g. horizontally and vertically). This is analogous to two cylindrical lenses or the two focusing mirrors in a Kirkpatrick-Baez system. The two MLLs must be optimized for the same photon energy but manufactured with focal lengths whose difference is equal to the separation of the lenses. Using two crossed MLLs results in a lens system with a square or rectangular aperture. For a square aperture the point spread function is the product of two sinc-functions of the coordinates in the two lenses focusing direction. Using the Rayleigh criterion, the spatial resolution $\Delta_{h,v}$ is equal to $\Delta_{h,v} = 0.5\lambda/\text{NA}_{h,v}$ [40]. The constant factor (0.5) corresponds to the first zero of the sinc-function of the point spread function [41]. Since when operating in their diffracting condition each lens splits the beam into a zero and a focusing order, the two crossed lenses form four beams altogether: an transmitted zero order beam; a horizontal line focus from the focusing order of vertically-focusing lens with the zero order of the other; a vertical line focus from the opposite combination of orders; and the two-dimensionally focused beam. For off-axis lenses, in the focal plane, all four beams are separated. In the far field (of the focus) the two line foci diverge into linear diffraction orders and the two-dimensional focus diverges into the inverted (square or rectangular) pupil of the lens pair.

The ability to manufacture the thin layers required for high numerical apertures depends on both the deposition process control and on the materials used. In the study presented here we used WC/SiC throughout, except for one MLL with a smaller NA, where we used W/SiC. The WC/SiC system is a novel material combination with many beneficial properties [42]. In a previous study a focused spot size of 8.4×6.8 nm^2 [31] at 16.3 keV was achieved with MLLs consisting of WC/SiC. Both WC and SiC remain amorphous over the whole range of the layer periods, avoiding wavefront errors that arise due to a transition from an amorphous to a crystalline structure in the W layers [38]. The multilayers used here were prepared in DESY's x-ray multilayer deposition laboratory as described previously [38, 43]. Each MLL was cut from a multilayer prepared in a separate deposition run; hence, four different deposition runs were required for two energies and two sets of 1D lenses. Design pameters of the MLLs are listed in Table 1.

For both sets, the MLL with the shorter focal length was mounted to focus the beam horizontally, while the one with a longer focal length focused the beam vertically. We are naming the lenses designed for 17.3 keV "1h" (horizontally focusing) and "1v" (vertically focusing). The MLLs of the set used at 34.5 keV are named "2h" and "2v".

The optimal lens depth depends strongly on the photon energy and on the contrast of the optical constants of the multilayer materials. The layer period and the volume fraction of high Z material in each bilayer of the multilayer, denoted here as Γ, have a weak influence on the

optimal lens depth [30]. To investigate this dependency and to fabricate MLLs with maximum efficiency, multislice beam propagation simulations as a function of the optical depth of MLLs optimized for 17.3 keV and for 34.5 keV were performed [44, 45] Added refs, deleted Appendix. In the simulation, each bilayer consisted of equal thicknesses of W and SiC, or WC and SiC, respectively, for the two photon energies. That is, $\Gamma = 0.5$. In our simulations, we assumed materials densities $\rho_{\mathrm{W}} = 19.3$ g cm^{-3}, $\rho_{\mathrm{WC}} = 13.8$ g cm^{-3} and $\rho_{\mathrm{SiC}} = 2.64$ g cm^{-3} where the subscripts indicate the material. These values were obtained by fitting small angle x-ray diffraction scans of periodic WC/SiC multilayers deposited under the same conditions [42]. The retrieved densities are, as expected, lower than the respective bulk densities ($\rho_{\mathrm{WC,bulk}} = 15.6$ g cm^{-3} and $\rho_{\mathrm{SiC,bulk}} = 3.21$ g cm^{-3} [46, 47]). The efficiency as a function of optical depth shows the damped oscillation characteristic of dynamical diffraction and the optimum efficiency at half the Pendellösung period. Using the aforementioned densities, we calculate the optimum efficiency of 59 % for a 7.5 μm thick MLL at 17.3 keV. Due to positioning errors in the FIB preparation process the actual optical depths of our MLLs were 7.0 μm and 6.5 μm (horizontal and vertical lens), respectively. The Pendellösung period is inversely proportional to the optical constants and hence the material density. The fitted densities have a relative error of up to 15 %, resulting in a 15 % relative error for predicting the optimum depth). The dependence of the optimum depth on the thickness ratio Γ of the materials is weak, with a 20 % change in Γ leading to an increase of the optimum thickness by 8 % as determined by simulation.

The MLLs designed for 34.5 keV have longer focal lengths and smaller numerical apertures (see Table 1), which have correspondingly smaller tilts of the layers. In fact, Eq. (1) indicates that from the entrance to the exit surface, the layer thickness should change by only 0.01 %. We approximated this with flat layers so no mask was used when preparing these MLLs. Assuming $\rho_{\mathrm{W,bulk}} = 19.3$ g cm^{-3} for W (bulk density) and $\rho_{\mathrm{SiC,bulk}} = 2.64$ g cm^{-3} for SiC an optimal depth of 12.2 μm should give an efficiency of 85 %. The optical depths of the MLLs were however measured to be much thinner (8.5 μm and 9.0 μm, respectively).

3. Experimental

3.1. Experimental setup

Experiments for lens characterization and for the applications presented in this paper were performed at the beamline ID06 at the European Synchrotron Research Facility (ESRF, Grenoble, France). The beam was monochromatized to 17.3 keV or 34.5 keV by a Si (111) double crystal monochromator in Bragg-Bragg geometry and subsequently pre-focused with a CRL transfocator consisting of a stack of eight 2D-focussing Be lenses with 200 μm diameters radius-of-curvature, placed 38.7 m downstream from the source. The end station was located approximately 58 m downstream from the source and offered a highly stable setup due to an underlying granite block with a mass of 20 tons. A CRL with 25 2D-focussing Be lenses with apex radius-of-curvature 50 μm and a distance between lenslets of 2 mm was placed as a condenser before the MLLs to increase the flux. The resulting focal length at 17.3 keV was 0.78 m.

The vertically and horizontally focusing MLLs were located on the same mount, which could be oriented to match two configurations. In the first configuration, the MLLs focus the incident beam to a spot (an image of the source), requiring the $2f$ wedge to converge in the downstream direction. This is the usual arrangement for scanning microscopy, although employed here primarily for wavefront characterization of the lenses and for projection microscopy. We refer to this as the "nanoprobe" configuration. In the "full-field imaging" configuration the MLLs were rotated by 180° such that the wedge apex is in the upstream direction for efficient acceptance of rays scattered from an object located slightly upstream of the focal plane of the lens. The mount could be further translated in three directions and rotated about two axes (pitch and yaw). The alignment of the lenses was carried out in the nanoprobe configuration. To align the MLLs relative to each other, the MLL with the longer focal length (vertically focusing) was placed on a

hexapod (on the common mount), with six degrees of freedom. The hexapod had a repeatability of 15 nm for up to 1 mm travel range. A first detector was located 0.13 m downstream from the MLLs to record transmission images of the MLLs. This detector comprised a scintillator screen coupled by a visible light microscope to a Frelon 2k CCD camera. The effective pixel size was 1.24 μm. A second, similar detector using a pco.2000 CCD camera, was placed 0.41 m or 0.63 m downstream from the MLLs and was used for recording the x-ray microscopy images (Fig. 2). This was also a scintillator-based detector with a 10× objective, which resulted in an effective pixel size of 0.74 μm.

3.2. Imaging geometries

We explored the use of the MLLs for projection imaging in two different geometries: one with a real source and one with a virtual source, and for direct imaging where the lens forms an image of the object on the detector. These three geometries are illustrated in Figs. 2(a), 2(b) and 2(c), respectively.

3.2.1. Projection holography with a real source.

In the nanoprobe configuration an incident collimated beam parallel to the optical axis is brought efficiently to a focus, as per the MLL wedge design discussed above and illustrated in Fig. 1(a). A transmission hologram of an object is obtained by placing it into the diverging beam downstream of the focus. The divergence magnifies the projected hologram so that features much smaller than the detector pixel size can be discerned. The divergence also ensures that the projection hologram is recorded in the near field. The resolution to which an image can be reconstructed depends in this case on the extent of the secondary source formed by the MLLs [48, 49].

In this work, we have used this mode of imaging for wavefront characterization as described below. Specifically, the sample is located a distance L_1 downstream of the focus and the Fresnel diffraction intensity distribution is recorded on the detector located a distance L_2 from the sample, with a magnification of 78 given by the geometric factor $M = (L_1 + L_2)/L_1$. The Fresnel diffraction pattern of an object of transmission $\Psi(r)$ formed with a diverging spherical wave is equivalent to that formed by plane-wave illumination of a magnified object $\Psi(r/M)$ but recorded a distance ML_2 from the object [50]. The Fresnel number of the diffraction of an object of width w is thus equal to $(Mw)^2/(\lambda M L_2)$. In our measurements, $L_2 = 400$ mm, $M = 78$, giving a Fresnel number of 960 for an object of width of 19 μm and wavelength of 0.72 Å(17.3 keV). For lens alignment and aberration characterization, the lenses were first positioned to obtain a common focus, eliminating horizontal-vertical astigmatism. This was achieved by first roughly adjusting the distance between the lenses to give equal magnification of the projection hologram in the vertical and horizontal directions, and then further adjustment was carried out by sensing the wavefront through the method of speckle tracking [51]. Furthermore, the orthogonal astigmatism aberration (45°-astigmatism) was reduced by aligning the roll of the horizontal lens located on the hexapod [52] until the images of the line diffraction orders were orthogonal to each other, using the orthogonality of the pixels of the detector as the reference. However, the line diffraction orders recorded on the detector have a width equal to the physical aperture size of the respective MLL, which can be up to 59 pixels for the investigated MLLs. Consequently, a residual deviation from 90° between the transverse focusing directions is still present after aligning (see Section 4.2).

3.2.2. Projection holography with a virtual source.

In this second projection geometry, illustrated in Fig. 2(b), a virtual source is used. The entire MLL stage is inverted to orient the lenses in the so-called full-field configuration where the apexes of the lens wedges are downstream of the lenses. An incident collimated beam, when parallel to the optical axis, diffracts into the negative diffraction order of each lens, providing a divergent

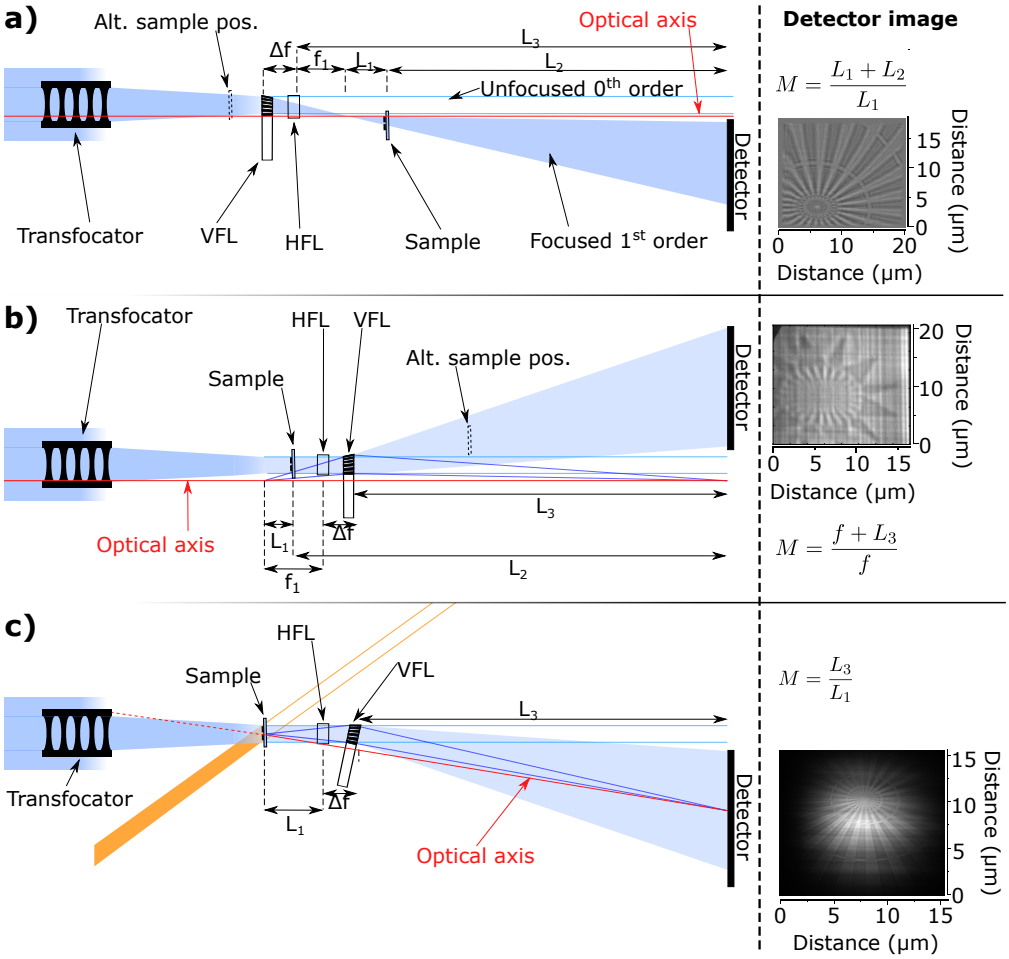

Fig. 2. Three kinds of imaging modes were used in two configurations of the MLLs. In the "nanoprobe" configuration the vertices of the MLL wedges lie downstream of the lens (a) and in the "full-field" configuration they lie upstream (b, c)Added reference [53]. (a) A sample placed in the diverging beam downstream of beam focus in the nanoprobe configuration forms a projection hologram (a magnified near-field diffraction pattern of the object). Alternatively, the sample can be placed upstream of the lenses (Alt. sample pos.). (b) Another projection holography mode is obtained in the "full-field" configuration where a collimated incident beam parallel to the optical axis is diffracted into a negative (diverging) order. The sample may again be placed upstream of the MLL (as shown) or downstream (Alt. sample pos.). The positive diffraction order in this configuration forms a direct image of an object in a small field near the optical axis (blue rays). (c) In the direct imaging mode with bright field illumination, the lens is tilted so that the incident rays pass both through the object field and the lens aperture (whereby the lens operates in its positive diffracting order). A magnified image is formed on the detector. In dark-field direct imaging, the incoming beam (orange) is directed away from the lens aperture and the image is formed by rays diffracted by the sample (blue). The right column shows cropped detector images obtained in the respective configurations. For all depicted configurations, the sample was a Siemens star and distances on the detector image axes refer to object space.

lens. This is a result of the asymmetry of the MLLs introduced by the wedge. Rays parallel to the optical axis intersect layers at the same incidence angle no matter whether impinging from one side of the lens or the other. However, in the reverse direction, instead of reflecting from the "underside" of the layers as depicted in Fig. 1(a), rays are reflected away from the optical axis. Since the Bragg angle is exactly the same, the diffraction efficiency is the same for the positive (converging) and negative (diverging) focusing orders.

Similar to projection holography with a real source, an object can be placed downstream or upstream of the lens to form a magnified projection hologram. With the object placed downstream, the magnification is as described above and given by $M = (L_1 + L_2)/L_1$ where now L_1 is the distance of the object to the virtual focus. Again, the diffraction distance for the equivalent "standard" collimated-beam diffraction geometry, is ML_2. When the object is located upstream of the lens and illuminated by a collimated beam, as depicted in Fig. 2(b), then the diffraction is in fact initially "standard" and reaches the lens while still in the near field (apparent since the field width is set by the lens aperture). The action of the lens is to expand this diffraction by a factor $M = (L_3 + f)/f$ (where L_3 is the lens to detector distance) and to give a further propagation that, together with the first, would be equivalent to diffraction of the magnified object propagated over a distance $M^2L_1 + ML_3$. Both L_3 and f are different for the two lenses employed in each set, which causes a different magnification along the horizontal and the vertical direction, respectively. Fig. 2(b) shows a projection hologram of a Siemens star.

Note that when operating as a diverging lens for an incident parallel beam, the wedged MLL can simultaneously form a real inverted image of an object close to the optical axis with the positive (converging) diffracted order. This is shown for the blue rays in Fig. 2(b). Since the MLLs are designed with a $2f$ wedge (for focusing a collimated beam), such direct imaging is optimized for forming a real image at infinity (with the object located a focal distance from the lens). However, the angular acceptance of the diffracting layers of the MLLs allows for efficient diffraction from rays originating from positions slightly away from the focus as well (see also the discussion below about the field of view). Thus, high magnifications can be tolerated. The direct image is centered on the optical axis and thus does not overlap with the projection hologram formed using the negative order. The image will actually be a dark-field image since the incident illumination passing through the object, parallel to the optical axis, will not pass through the off-axis aperture of the MLLs. That is, the zero spatial frequency of the object lies outside the pupil of the lens.

3.2.3. Direct imaging.

The ability for the lens to form a direct image when the wedge vertices are located downstream is indeed why we refer to this as the "full-field" configuration [53] Added ref. In general, when used to form a real magnified image of an object, the lenses will not be placed to fulfill the diffraction condition of the negative order, but rather adjusted to achieve the desired imaging conditions. This direct imaging configuration is illustrated in Fig. 2(c). Here, just as for a thin lens, the image is inverted with respect to the optical axis, even though the MLLs are formed as off-axis portions of full lenses. The full-field image is formed with two one-dimensional lenses of different focal lengths (equivalent to two cylindrical lenses) resulting in different magnifications in the horizontal and vertical directions. That is, the image is anamorphic. Taking each lens to be an ideal thin lens (neglecting its thickness), in our studies, the horizontal magnification was $M_h = 635\,\text{mm}/9.5\,\text{mm} \approx 67$ and the vertical magnification $M_v = 630\,\text{mm}/13.7\,\text{mm} \approx 46$.

The contrast of the image depends on the illumination. Figure 2(c) shows that bright-field or dark-field direct imaging can be realized, depending on whether the incident beam illuminating the object (within the field of view close to the optical axis) is directed into the pupil of the lens or not. In the case of bright-field microscopy the contrast depends mostly on the transmission of the object since the optical transfer function of the lens overlaps the zero spatial frequency of the

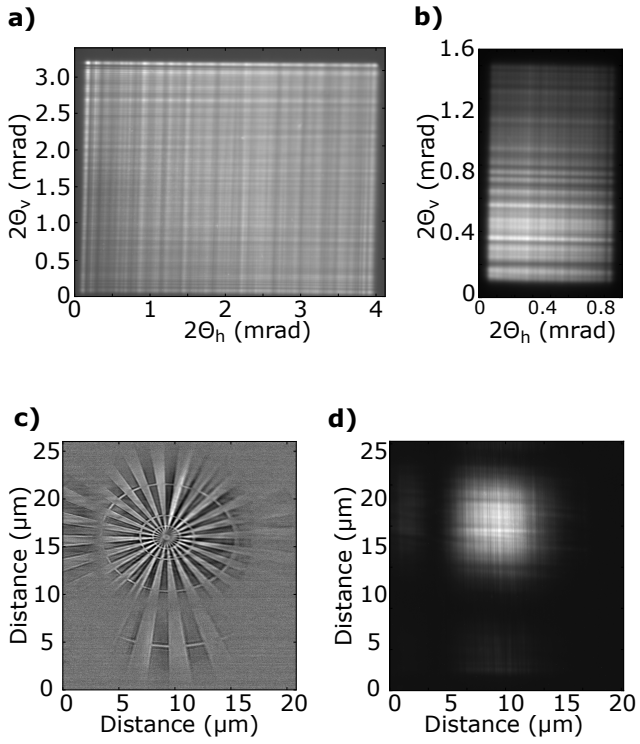

Fig. 3. The intensity of the lens pupil in the projection imaging configuration of Fig. 2(a) at (a) 17.3 keV and at (b) 34.5 keV. The horizontal and vertical axes are the horizontal diffraction angle $2\theta_h$ and the vertical diffraction angle $2\theta_v$, respectively. A flat-field corrected bright-field real image of a test object at 17.3 keV is depicted in (c). The intensity of the field at 17.3 keV without the sample present is shown in (d). The axes in both (c) and (d) are distances in object space. For all intensity plots the grey scale is linearly scaled between 0 counts (black) and the maximum intensity (white).

object. By moving the sample slightly off focus, phase contrast is obtained (defocus contrast). In dark-field imaging, only rays scattered by the sample into the pupil of the MLLs form the image, which excludes the zero spatial frequency. The details of the image formation depend on the coherence of the illumination [54]. For hard X-rays, we are particularly interested in forming images from X-rays Bragg scattered from crystallites in the sample which happen to be oriented in the appropriate reflecting condition [55]. This requires setting the illumination angle (in practice, tilting the optical axis of the lens) to match the chosen Bragg angle.

A key feature of an MLL objective used in the direct imaging mode is that the diffraction properties of the lens cause vignetting of the image field. The layers are oriented to reflect rays originating from a point in the object (with an object to lens distance L_1 slightly larger than f) on the optical axis. Rays originating from points in the sample plane further away from the optical axis will be diffracted by particular layers in the lens with less efficiency, as those rays move out of the rocking-curve acceptance of the layers. This acceptance varies with the position on the lens. For the small diffraction angles of MLLs this rocking curve width varies inversely with the Bragg angle [56] and thus it is linearly proportional to the layer period, as well as being proportional to the difference in optical constants of the layers [30]. Thus, as the object point moves away from the optical axis, the effective NA of the lens is reduced as more layers (starting from the thinnest) exclude rays. The extent of the field is ultimately limited by the acceptance of

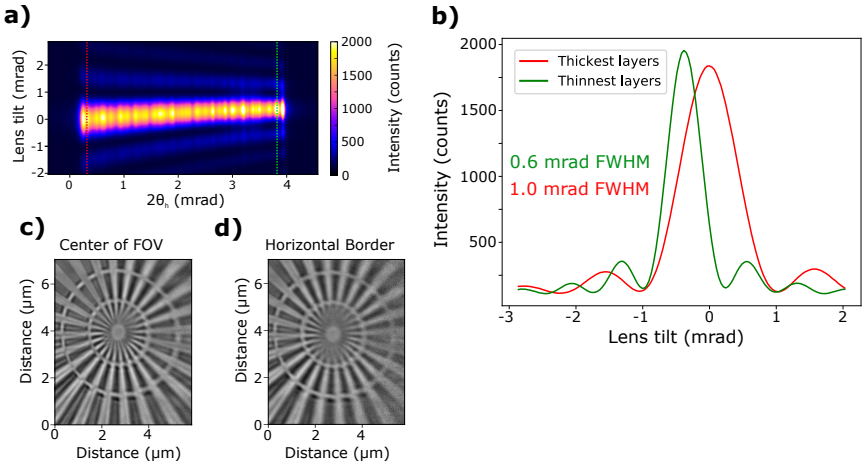

Fig. 4. The diffraction efficiency as a function of the lens tilt (a). The investigated lens is the horizontally focusing MLL designed for 17.3 keV. Intensity lineouts along the lens tilt axis have been extracted for the lens part with the thickest layers (red dotted line) and for the thinnest layers (green dotted line). The retrieved lineouts are shown in (b). A cropped full field image of the center of the Siemens star test sample is shown, where the features were located at the center of the FOV (c). The same sample features after moving to the horizontal border of the FOV, while still being centered in the vertical direction (d).

the thickest layers. The full aperture of the lens, and hence the full resolution, is only achieved within the acceptance of the thinnest layers, with the field of view depending on the rocking curve width $\Delta\theta$ as FOV $= L_1\Delta\theta \approx f\Delta\theta$. The vignetting is analogous to that of an ideal thin lens of finite NA with an entrance pupil located between the object and the lens, such that the full NA of the lens is only achieved for a point on axis. The FOVs of the investigated MLLs, obtained from the measured rocking curve width, can be found in Table 1. An experimental quantification of this effect and its impact on the imaging resolution is given in Section 4.1 (Fig. 4).

4. Optical performance

Determination of key optical performance parameters such as the spatial resolution, FOV and the efficiency of the MLL was performed by tests in the nanoprobe configuration. A highly coherent beam was used in order to exploit methods such as speckle tracking and ptychography.

4.1. Basic performance of the MLLs

Image formation in a microscope can be described by Fourier optics [57]. A coherent full-field image, formed for example by illumination of a transmitting sample by a collimated beam, is given by the square modulus of the convolution of the object's transmission function and the point spread function of the lens [57]. The point spread function in this case is the Fourier transform of the complex-valued lens pupil function, which ideally should be of uniform amplitude and phase within the angular acceptance of the lens. Note that due to the vignetting described above, the pupil function varies with the position of the point in the field, and the formalism of Fourier optics holds over a limited region called the isoplanatic patch.

In the nanoprobe configuration, a map of the square modulus of the lens pupil function for the on-axis field point can be obtained simply from the far-field diffraction pattern recorded on the detector without any object in place, as formed using collimated illumination parallel to the optical axis. (The pupil for other points in the field can be obtained by carrying out the same procedure with different lens tilts.) The condition for far field diffraction is fulfilled for

a propagation distance $z_F > 2D^2/\lambda$. Here D represents the beam width in the focus. For a non-aberrated lens D is smaller than λ/NA [41], giving $z_F > 2\lambda/\mathrm{NA}^2$ or twice the depth of focus. Therefore, the condition for far-field diffraction requires $z_F > 56$ μm for the MLLs designed for 17.3 keV and $z_F > 450$ μm at 34.5 keV. With our detectors (0.74 μm pixel widths), we set the distance in the nanoprobe configuration to 0.41 m, which gives about (2000×1730) and (450×770) pixels across the projected lens pupil as depicted in Figs. 3(a) and 3(b), respectively for these two photon energies. At this distance, the pupil of the horizontally focusing MLL (lens 1h at 17.3 keV) approximately covers the full width of the detector (2048 pixels) and it enables projection images to be obtained with high magnification. The numerical apertures of the individual MLLs are given in Table 1.

As shown in Fig. 3, the pupil intensities for 17.3 keV (Fig. 3(a) and 34.5 keV (Fig. 3(b)) show a checkerboard pattern. Apart from this pattern the pupil intensity of the set (1h,1v) are uniform at 17.3 keV, indicating constant efficiency (Fig. 3(a)). The pupil intensity of the set (2h,2v) at 34.5 keV shows an intensity gradient with highest intensity in the bottom left corner (Fig. 3(b)). This intensity gradient is attributed to a slight mismatch of the optimal photon energies for the individual MLLs of the set (2h,2v). The rectangular pupil shape (instead of a square) in Fig. 3(b) is due to the difference in the numerical apertures of the used MLLs (0.4 mrad (2h) vs. 0.7 mrad (2v), see Table 1).

A bright-field image - with the MLL used as an objective - of a test object at 17.3 keV is depicted in Fig. 3(c) for magnifications of 67 in the horizontal direction and 46 for the vertical. The Siemens star pattern is made from 600 nm thick gold, and with 50 nm smallest features. Anamorphism of the image is clearly seen due to the different magnifications in the two directions. The magnifications would suggest an anamorphism of $67/46 = 1.49$, which matches the observed anamorphism of 1.4 ± 0.1. The field of view is finite, and the image vignetting is seen to follow the shape of a distorted sinc function with visible side lobes along the horizontal and vertical axes. The illumination without the sample (flat field) is shown in Fig. 3(d). The vignetting of the image is caused by the finite angular acceptance of layers in the MLLs, limited by the rocking curve width as described in Section 3.2.

Figure 4(a) shows the measured diffraction efficiency of the positive diffraction order (obtained in the nanoprobe configuration), mapped as a function of the lens tilt, for the horizontally focusing MLL designed for 17.3 keV (1h). The measured widths are 1.0×10^{-3} FWHM (radians) for the thickest layers and 0.6×10^{-3} for the thinnest layers. With a focal length of 9.5 mm, this corresponds to a FOV at the object plane of 9.5 μm and 5.7 μm, respectively for these layers. That is, we would expect full resolution to be achieved over a FOV of 5.7 μm. Figs. 4(c) and 4(d) show cropped full field images of the finest features of the Siemens star test sample. For Fig. 4(c), we moved the sample so that the features were in the center of the FOV and therefore could be imaged with optimal resolution. In Fig. 4(d), the sample was moved horizontally to image the features at the horizontal border of the FOV, while the vertical side was still centered. The vertical resolution (sharpness of horizontal lines) was unaffected by this sample shift, while the horizontal resolution (sharpness of vertical lines) is worse due to the lower effective NA. This confirms the behavior described in section 3.2.3. The overall FOV of the investigated MLLs, obtained from the measured rocking curve width, can be found in Table 1.

4.2. Wavefront characterization and resolution

We carried out wavefront measurements to characterize the aberrations of the MLLs by two different methods: ptychography [58, 59] and speckle tracking. Both methods are carried out in the "nanoprobe" configuration. In the former, far-field diffraction patterns of a defocused Siemens star pattern were recorded. In speckle tracking the defocus is increased and near-field projection holograms are instead recorded for different transverse shifts of the object. An iterative speckle tracking algorithm recovers the wavefront aberration and the corrected projection hologram of

the object [51].

Even for perfectly manufactured MLLs, the following aberrations can be present due to alignment:

- The parabolic wavefront curvature of a spherical wave (defocus) is dominant, because the sample has to be located away from the focal plane in order to obtain projection holograms.
- 0-90°-astigmatism occurs if the focal plane of the horizontally and the vertically focusing MLLs are not the same.
- 45° astigmatism occurs if the lenses are not orthogonal to each other [52, 60].

Other aberrations are due to manufacturing errors of the MLLs and cannot generally be corrected by alignment.

When analyzing the aberrations, we start by subtracting the aforementioned aberrations from the reconstructed wavefront. This can be done by defining a set of Legendre polynomials that are orthogonal on a rectangular pupil, similar to Zernike polynomials on a unit disk. These are then fitted to the measured wavefront so that the aforementioned primary terms can be subtracted. As the calculations are performed on a finite grid, the numerical polynomials are not perfectly orthogonal. To overcome this, a numerical Gram-Schmidt orthogonalization is carried out [24].

Figure 5 plots the pupil wavefront reconstruction of the lens pair designed for 17.3 keV (1h,1v), obtained via far field ptychography [59] with a Siemens star sample. For ptychography, the defocusing distance was set to 1010 μm. Because horizontal and vertical focusing is performed by individual, orthogonal lenses, the obtained wavefront is expected to be separable such that the phase $\phi(x, y)$ can be written as the sum of the horizontal and vertical phase:

$$\phi(x, y) = \phi_h(x) + \phi_v(y) \tag{2}$$

Nevertheless, a small residual 45° astigmatism (added ref) [52] was present due to a slight misalignment of the lenses of about 0.2°. Only after removing this 45° astigmatism, the wavefronts can be easily separated. The resulting phase profiles are plotted in Fig. 5(b). The shape of the profile is similar to coma in Zernike polynomials and indicates the existence of two foci on different planes for each lens. By fitting and removing one of the parabolas one can obtain the pupil wavefront corresponding to one of the foci. The resulting curve shows a phase roll-off at higher diffraction angles. Similar aberrations were reported previously for an unrelated set of MLLs and can be attributed to the thinnest layers being systematically too thick [31]. For the horizontally focusing MLL (1h), the measured phase error is approximately 60 radians peak to valley. On average, this is equivalent to a phase error of 0.01 radians per period. Therefore, for periods on the order of 10 nanometers, the error per period is approximately 0.03 nm (before: It is estimated that the thickness error is much less than 0.1 nm for periods of the order of 10 nm.).

Figure 5(b) shows the separated wavefront profiles obtained from speckle tracking. A comparison of the results obtained with speckle tracking and ptychography shows a good quantitative agreement. The mean absolute difference of the 2D wavefronts is 1.68 rad, which is approximately 16 % of the standard deviation of the 2D wavefronts.

The point spread function of the MLLs at 17.3 keV (1h,1v) is shown in Fig. 5(c) along with their 1D profiles (Fig. 5(d)). By fitting the central spot with a Gaussian function a focus size of $(34 \pm 1.5) \times (36 \pm 3.0)\,\mathrm{nm}^2$ FWHM is obtained, listed in Table 2. This value agrees well with a focus size of 35 ± 5 nm obtained by analyzing the edge sharpness in the full field image. A perfect set of MLLs of this design would have a Rayleigh resolution of $18 \times 22\,\mathrm{nm}^2$. The discrepancy observed here is due to the already mentioned systematic mismatch between deposited and designed layer thicknesses, which in principle can be corrected by appropriate modification of the deposition parameters.

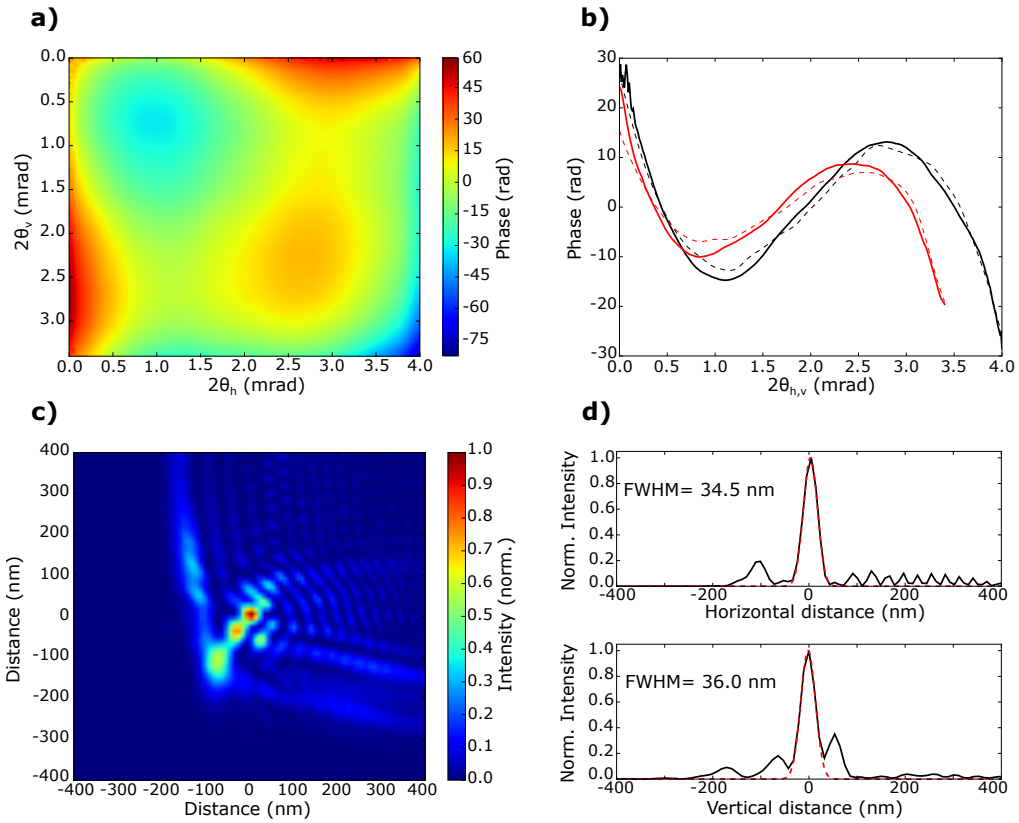

Fig. 5. Wavefront characterization af 17.3 keV. (a): 2D wavefront retrieved from ptychography after removing primary aberrations. (b): The separated horizontal and vertical wavefronts after removing 45° astigmatism. The black curves show the horizontal profile $\phi_h(x)$ and the red curves show the vertical profile $\phi_v(y)$ (Eq. (2)). The solid lines are the results from ptychography and the dashed lines were obtained from speckle tracking. (c): The intensity in the focal plane according to ptychographic reconstructions. (d): The respective horizontal and vertical profiles.

At 34.5 keV (lenses 2h,2v), the absorption contrast of the Au test sample is reduced by a factor of ~ 13 compared to the images taken at 17.3 keV. Even with this reduced contrast, it was still possible to track its features and to measure wavefronts with speckle tracking. Unfortunately, due to the lower coherence at this energy, ptychographic reconstructions did not give meaningful results. The 1D wavefronts, obtained as described above, are dominated by features from the MLL with larger NA, the lens focusing in the vertical direction. The focus spot was fitted with Gaussian curves with FWHM of $(114 \pm 7) \times (56 \pm 11)\,\mathrm{nm}^2$ along the horizontal and vertical directions, respectively. The optimal Rayleigh resolution of diffraction limited MLLs for the given NA is $40 \times 23\,\mathrm{nm}^2$ FWHM (Table 2).

4.3. Diffraction efficiency

Due to the limited dynamic range of the available detectors, the diffraction efficiencies of the MLLs were estimated by measuring the extinction of the lenses in projection geometry under various tilts, using the "Frelon 2k" camera. For a perfectly wedged MLL there exists a tilt angle at which all the layers fulfill Bragg's law. At this angle the transmitted intensity (0^{th} diffraction order) is reduced, because most of the rays diffract away from the detector (extinction)(Added

Table 2. Focal length, focus size (FWHM) and efficiency of the investigated MLLs.

Name	Energy (keV)	f (mm)	Theoretical spatial resolution (nm)	Experimental focus (nm)	Theoretical efficiency (%)	Experimental efficiency (%)
1h	17.3	9.5	18	34.5 ± 1.5	59	51
1v	17.3	13.7	22	36 ± 3.0	58	54
2h	34.5	37	40	114 ± 7	77	n.a.
2v	34.5	40	23	56 ± 11	79	n.a.

ref) [61]. Accordingly, the lens is more transparent at angles differing from this angle. This is illustrated in Fig. 6. To take into account absorption, it is necessary to measure the intensity of the direct beam I_0. With I_{df} being the dark field intensity without the beam, I_b the intensity at the Bragg condition and I_{nb} the intensity when the Bragg condition is not fulfilled, the diffraction efficiency is given by:

$$E_{abs} = \frac{I_{nb} - I_b}{I_0 - I_{df}} \tag{3}$$

The resulting efficiencies, with absorption taken into account, are listed in Table 2. For set (2h,2v) no data for efficiency measurement was recorded. The diffraction efficiency at 17.3 keV is 51 % (horizontal lens) and 54 % (vertical lens) and the combined efficiency of the crossed lenses is 27.3 %. The efficiencies of these two individual MLLs are similar. The small difference is within the error bar of the measurement, which is about 5 %. The total experimental efficiency (considering two overlapping lenses, diffraction and absorption) is 27.3 %, which is lower than the simulated 34 % at 17.3 keV. We attribute this loss in efficiency to the observed aberrations including a non-perfect shape of the wedged layers. The method we used to calculate the efficiency also assumes that all rays deflected by the lens contribute to the focus. Due to aberrations this may not be the case. Hence our estimation might overestimate the total efficiency. Moreover, this measurement assumes that rays of all higher diffraction orders are contributing to the focus. Even though heavily supressed for wedged MLLs, these higher orders lead to an overestimation of the total efficiency.

5. Demonstration of direct beam applications

In the past, several successful demonstrations have been made of the use of MLLs for projection microscopy at x-ray energies of 9 to 12 keV [61, 62]. To our knowledge, however, there has been little work on direct imaging applications. In this section, we demonstrate the use of the MLLs for magnified direct imaging in the bright and dark-field configurations, both illustrated in Fig. 2(c).

The two proof-of-concept studies relate directly to the vision of 3D multiscale materials science pursued at the hard x-ray microscope ID06 at ESRF. Here the resolution-limiting element currently is the x-ray objective. For studies above 20 keV, CRLs [5, 19, 63] have been the optics of choice. Aberrations in CRLs limit the experimental resolution to approximately 100 nm. In comparison, MLLs with reduced manufacturing errors, a higher NA and a higher efficiency open the door to local imaging with a much-improved spatial resolution.

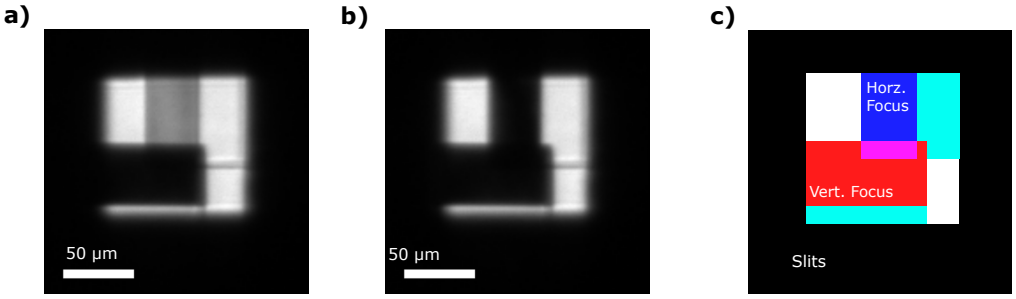

Fig. 6. Transmission images of the two crossed MLs. The vertically focusing MLL is tilted to match the Bragg angle (bottom black rectangle). The slits (outer black square) are set to match the beam to the lens pupils. The horizontally focusing MLL tilt is in a) set to an arbitrary angle, away from Bragg angle (appearing as the top grey rectangle) and in b) set to the Bragg angle (black rectangle). A schematic of the layout is shown in c). The horizontally focusing lens is shown as a blue square, the vertically focusing lens as a red square and the overlapping region is purple. All lenses are mounted on a silicon substrate, which is depicted as cyan squares.

5.1. High resolution bright field imaging

Figures 7(a)-7(c) presents flat-field corrected data from the bright-field study at 17.3 keV using the Siemens star object with different amounts of defocus obtained by adjusting the position of the MLL along the optical axis. The horizontal magnification was measured to be 67, while according to Table 1 the NA for the horizontal lens is 2.0×10^{-3} and the focal length 9.5 mm. The field of view is measured to ~ 7 μm FWHM, to be compared with a predicted value of 9.5 μm. The images clearly document the feasibility of using of MLLs for direct beam studies. Also clearly visible is the astigmatism, e.g. in Fig. 7(b) where the MLLs is positioned in the middle between the horizontal and vertical focusing points. It is illustrative to compare the optical specifications of this setup to the equivalent setup with a Be CRL as objective. For the same focal length and magnification, and with the available specifications of a radius-of-curvature of 50 μm and a thickness of 2 mm, such an objective would require the use of 157 lenslets, be 31 cm long, have an NA of 0.42×10^{-3} (HWHM) and a field-of-view of 87 μm (rms) [55]. Again, we note the compromise between NA and FOV.

The contrast obtained by translating the lenses along the optical axis gives rise to fringes in both the vertical and horizontal directions around the edges of the spokes of the Siemens star object, as seen in Fig. 7(a)-7(c). This is consistent with defocus phase contrast, including the reversal of the contrast of the fringes on opposite sides of focus. To quantify the contrast, we performed a set of partially coherent wavefront simulations for each position of the MLLs, replicating the experiment in the simulations, see Figs. 7(d)-7(f). The wavefront simulations were performed using a Fractional Fourier Transform (FrFT) approach, described in [64]. We initially assumed a fully coherent incoming plane wave being transmitted through the Siemens star, with the exit field immediately after the object being determined by the attenuation and phase shift corresponding to 600 nm thick Au features of the object. From the magnification of the image, we established the focal lengths of the horizontal and vertical MLLs to be 9.9 mm and 13.1 mm, respectively. The wavefront propagation simulations take the astigmatism into account.

The wavefront propagation model captures the main features of the experiment, in particular the reversal of fringe contrast, but the contrast is less pronounced experimentally. We see this as an indication that the incoming beam is only partially coherent, and introduce a horizontal and vertical coherence length. By optimizing the correspondence between experiment and model, the estimated values of these coherence lengths are 65 nm and 130 nm respectively. As an

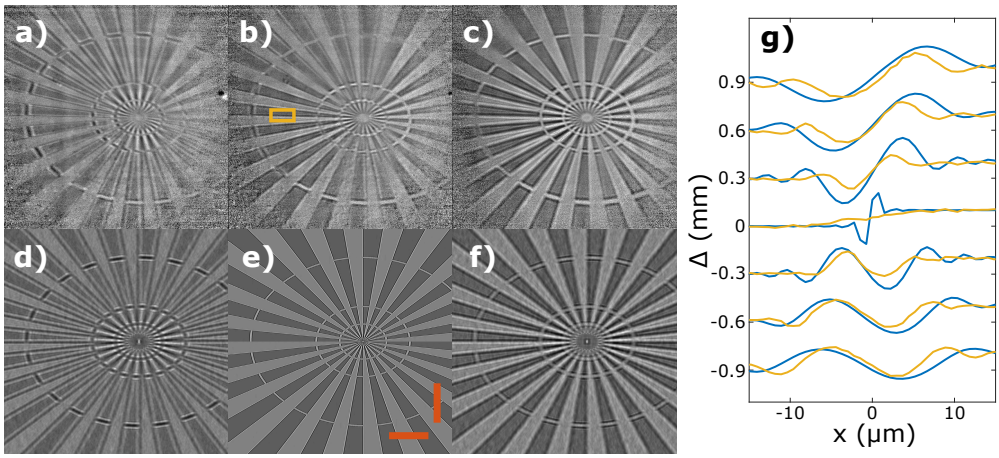

Fig. 7. Bright-field direct imaging of the Siemens star with the MLL objective being translated along the optical axis. (a-c) experimental images for defocus distances of 0.6 mm, 0 mm and -0.6 mm. (d-f) corresponding partial coherent wavefront simulations with the same three distances. The orange scale bars in (e) are 2 μm in the object plane. (g) shows the vertical line profile obtained from the position indicated by the yellow box in (b). The seven curves correspond to relative sample-objective distances of -0.9, -0.6, -0.3, 0, 0.3, 0.6 and 0.9 mm, respectively, with the shortest distance at the bottom. Corresponding simulations with a vertical coherence length of 130 nm are shown in blue.

example of the results in Fig. 7(g) we compare the intensity profile across a horizontal edge. The correspondence in position and amplitude of the fringes is seen as satisfactory.

These results point to a new way of performing high resolution phase contrast studies with hard x-rays, compared with the projection holography shown above. Phase retrieval for such a set of images taken through focus may be obtained using solutions based on the transport of intensity equation [65]. Notably, for the set-ups demonstrated here it is not required to place any optical elements or a detector close to the sample to probe the nearfield, and when employed in the direct-imaging configuration, phase contrast can be easily combined with diffraction contrast imaging, as discussed below in section 5.2.

As a heuristic approach, we determined the spatial resolution of the microscope by fitting the horizontal and vertical edges with an error function. Based on fits at the optimal position, we estimate the RMS resolution to be (37.4 ± 8.8) nm and (109 ± 21) nm.

5.2. High resolution dark-field microscopy

The dark field direct beam imaging modality shown in Fig. 2(c) is known as "Dark-field X-ray microscopy". It is a method that has been recently applied for non-destructively mapping the structure of deeply embedded crystalline elements in 3D [12]. Placing a CRL objective in the diffracted beam generates a magnified projection image of a large volume. Similar to the operations of a transmission electron microscope, one can combine direct space mapping in the image plane [55] with reciprocal space mapping in the back focal plane [66]. It is an invaluable tool for materials science, and has to-date been applied to study a range of materials and phenomena [12–15]. Crucially, it enables movies of structural evolution with temporal resolution on the order of seconds to minutes. As already mentioned, the current limitation is the performance of the CRL objective.

As a proof-of-principle, we mapped the lattice orientation distributions around the ferroelectric domain walls in a 150 μm-thick crystal of $BaTiO_3$. These materials are pervasive in optical,

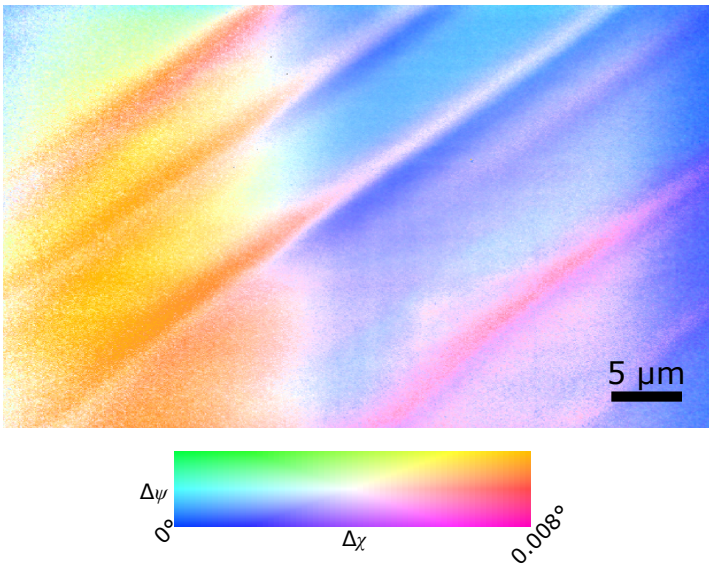

Fig. 8. Dark-field direct imaging using the MLL as objective. Shown is a projection image of lattice misorientations around ferroelastic/ferroelectric domains in a $BaTiO_3$ single crystal. The misorientation is read as the color according to the colorscale below.

electromechanical, and dielectric applications, where the nucleation, growth, interaction and annihilation of their ferroelectric domain walls are crucial to their functionality. The magnitude, directions and spatial extents of the lattice distortions caused by the domain walls is poorly understood, in large part due to the fact that the vast majority of the domain walls are buried in the bulk material and inaccessible to conventional characterization approaches.

Here, dark-field x-ray microscopy on the (011) reflection of the sample allows these lattice distortions to be mapped directly, while the use of the MLL enables measuring maps with higher spatial resolution and at higher x-ray energies than previously attempted. Figure 8 shows a map of the average lattice misorientation from a projection through the crystal. The ferroelastic domain walls are clearly visible as the diagonal lines aligned with the (110) direction of the sample. In this map, the transition region between neighbouring domain orientations at the domain wall is in the order of 1 μm thick, in agreement with previous measurements of embedded domain walls using x-ray microscopy [15]. The map also shows a clear misorientation between the top and bottom parts of the image, which is likely attributable to an out-of-plane domain wall along (101)-type planes. This allows the local lattice distortions at the intersection of the (101)- and (110)-oriented domain walls to be investigated directly and in detail. Combined with the significantly improved spatial resolution afforded by MLLs, this opens the door to direct maps of complex domain topologies and their interactions in a variety of ferroic materials.

6. Conclusion

Multilayer Laue lenses were successfully used in x-ray microscopy experiments at 17.3 keV and 34.5 keV. A detailed lens characterization was performed in a projection imaging geometry. The pair of wedged MLLs designed for 17.3 keV focused the beam to $(34.5 \pm 1.5) \times (36 \pm 3)$ nm^2 with 51 % $\times$ 54 % efficiency. The wavefront of these lenses has been obtained with ptychography and an iterative speckle tracking algorithm. The results show good qualitative and quantitative agreement. Speckle tracking does not have strict coherence requirements and it was possible to also perform wavefront characterization for a set of MLLs at 34.5 keV with incoherent x-rays.

This characterization indicated a focus size of $(114 \pm 7) \times (56 \pm 11)$ nm^2 FWHM. Retrieved wavefronts of all investigated MLLs showed a high reproducibility of the residual wavefront curvature, caused by lens imperfections, which can presumably be corrected in future lenses.

After successful characterization, we realized a projection microscope set-up with MLLs serving as objective. It was shown that the field of view of the microscope is limited to approximately 9.5×15.1 μm^2 for the investigated set of MLLs designed for 17.3 keV and to 22.2 $\times$ 27.2 μm^2 for the 34.5 keV objective. The FOV is inversely proportional to the diffraction angle and is caused by the finite angular acceptance of the layers, given by the rocking curve width in the rocking curve. Hence, there is a compromise between large FOV and high resolution, which has to be taken into account. Furthermore, we demonstrated the use of MLLs for high resolution direct imaging. In the bright field mode, a series of exposures with the object on each side of the focus showed the expected sign reversal of the fringes at edges of the test sample, however the contrast was less pronounced than it would be for a fully coherent beam. Fractional Fourier Transform simulations were used to replicate the experimental conditions, which enabled us to estimate the horizontal and vertical coherence lengths of the incoming beam (65 nm and 130 nm).

Multilayer Laue lenses provide several advantages for dark-field microscopy, when compared to the use of CRLs, which are the state of the art optics at high energies. The aberrations are much reduced and the MLLs potentially offer spatial resolutions beyond the theoretical limit of the CRLs. Moreover, it is expected that the high angular coverage of an objective based on MLLs and the high focusing efficiency will lead to shorter exposure times.

Funding

We acknowledge support from Deutsche Forschungsgemeinschaft (DFG)(Gottfried Wilhelm Leibniz Program).
DanMAX, grant number 4059-00009B.
The ERC Advanced Grant d-TXM.
Travel grant by Danish instrument center Danscatt.

Acknowledgments

We would like to thank Sabrina Bolmer and Pavel Alexeev (DESY) for their help and technical support, Andrzej Andrejczuk (Univ. of Bialystok, Poland) for helpful and constructive discussions and ESRF for provision of beamtime. C. D. thanks D. M. Paganin for stimulating discussions on the field of view of thick lenses.

References

1. T. A. Lafford, J. Villanova, N. Plassat, S. Dubois, and D. Camel, "Synchrotron X-ray imaging applied to solar photovoltaic silicon," J. Phys. Conf. Ser. **425**, 192019 (2013).
2. G. Requena, P. Cloetens, W. Altendorfer, C. Poletti, D. Tolnai, F. Warchomicka, and H. P. Degischer, "Sub-micrometer synchrotron tomography of multiphase metals using Kirkpatrick-Baez optics," Scr. Mater. **61**, 760–763 (2009).
3. O. Betz, U. Wegst, D. Weide, M. Heethoff, L. Helfen, W. K. Lee, and P. Cloetens, "Imaging applications of synchrotron X-ray phase-contrast microtomography in biological morphology and biomaterials science. I. General aspects of the technique and its advantages in the analysis of millimetre-sized arthropod structure," J. Microsc. **227**(1), 51–71 (2007).
4. P. Villanueva-Perez, S. Bajt, and H. N. Chapman, "Dose efficient Compton X-ray microscopy," Optica **5**(4), 450–457 (2018).
5. C. G. Schroer, O. Kurapova, J. Patommel, P. Boye, J. Feldkamp, B. Lengeler, M. Burghammer, C. Riekel, L. Vincze, A. van der Hart, and M. Küchler, "Hard x-ray nanoprobe based on refractive x-ray lenses," Appl. Phys. Lett. **87**, 124103 (2005).
6. B. Lengeler, C. G. Schroer, J. Tümmler, B. Brenner, M. Richwin, A. Snigirev, I. Snigireva, and M. Drakopoulos, "Imaging by parabolic refractive lenses in the hard X-ray range," J. Synchrotron Radiat. **6**, 1153–1167 (1999).
7. J. C. da Silva, A. Pacureanu, Y. Yang, S. Bohic, C. Morawe, R. Barrett, and P. Cloetens , "Efficient concentration of high-energy x-rays for diffraction-limited imaging resolution," Optica **4**(5), 492–495 (2017).

8. H. Yan, N. Bouet, J. Zhou, X. Huang, E. Nazaretski, W. Xu, A. P. Cocco, W. K. S. Chiu, K. S. Brinkman, and Y. S. Chu , "Multimodal hard x-ray imaging with resolution approaching 10 nm for studies in material science," Nano Futures **2**, 011001 (2018).
9. A. Sakdinawat and D. Attwood , "Nanoscale X-ray imaging," Nat. Photonics **4**, 840–848 (2010).
10. J. C. Andrews, E. Almeida, M. C. H. van der Meulen, J. S. Alwood, C. Lee, Y. Liu, J. Chen, F. Meirer, M. Feser, J. Gelb, J. Rudati, A. Tkachuk, W. Yun, and P. Pianetta , "Nanoscale X-Ray Microscopic Imaging of Mammalian Mineralized Tissue," Microsc. Microanal. **16**(3), 327–336 (2010).
11. N. Nango, S. Kubota, A. Takeuchi, Y. Suzuki, W. Yashiro, and A. Momose , "Talbot-defocus multiscan tomography using the synchrotron X-ray microscope to study the lacuno-canalicular network in mouse bone," Biomed. Opt. Express **4**(6), 917–923 (2013).
12. H. Simons, A. King, W. Ludwig, C. Detlefs, W. Pantleon, S. Schmidt, F. Stöhr, I. Snigireva, A. Snigirev, and H. F. Poulsen, "Dark-field X-ray microscopy for multiscale structural characterization," Nat. Commun. **6**, 6098 (2015).
13. H. Simons, A. C. Jakobsen, S. R. Ahl, C. Detlefs, and H. F. Poulsen, "Multiscale 3D characterization with dark-field x-ray microscopy," MRS Bulletin **41**, 454–459 (2016).
14. A. C. Jakobsen, H. Simons, W. Ludwig, C. Yildirim, H. Leemreize, L. Porz, C. Detlefs, J. E. Daniels, D. Damjanovic, and H. F. Poulsen, "Mapping of individual dislocations with dark field x-ray microscopy," in review (2018).
15. H. Simons, A. B. Haugen, A. C. Jakobsen, S. Schmidt, F. Stöhr, M. Majkut, C. Detlefs, D. Damjanovic, and H. F. Poulsen, "Long-range symmetry breaking in embedded ferroelectrics," Nature Mater. **17**, 814–819 (2016).
16. E. Nazaretski, W. Xu, N. Bouet, J. Zhou, H. Yan, X. Huang, and Y. S. Chu, "Development and characterization of monolithic multilayer Laue lens nanofocusing optics," Appl. Phys. Lett. **108**, 261102 (2016).
17. R. Barrett, R. Baker, P. Cloetens, C. Morawe, R. Tucoulou, and A. Vivo, "Reflective Optics for Hard X-ray Nanofocusing Applications at the ESRF," Synchrotron Radiation News **29**(4), 10–15 (2016).
18. P. Kirkpatrick and A. V. Baez, "Formation of Optical Images by X-Rays," J. Opt. Soc. Am. **38**(9), 766–774 (1948).
19. A. Snigirev, V. Kohn, I. Snigireva, and B. Lengeler, "A compound refractive lens for focusing high-energy X-rays," Nature **384**, 49–51 (1996).
20. A. J. Fresnel, "Calcul de l'intensité de la lumière au centre de l'ombre d'un ecran et d'une ouverture circulaires eclairés par un point radieux," Œuvres Complètes d'Augustin Fresnel, Imprimerie Impériale, Paris (1866).
21. H. Mimura, S. Handa, T. Kimura, H. Yumoto, D. Yamakawa, H. Yokoyama, S. Matsuyama, K. Inagaki, K Yamamura, Y. Sano, K. Tamasaku, Y. Nishino, M. Yabashi, T. Ishikawa, and K. Yamauchi , "Breaking the 10 nm barrier in hard X-ray focusing," Nat. Phys. **6**, 122–125 (2010).
22. R. Hudec , "Kirkpatrick-Baez (KB) and Lobster Eye (LB) Optics for Astronomical and Laboratory Applications," X-Ray Opt. Instrum. **2010**, 139148 (2010).
23. Y. Suzuki, "Resolution Limit of Refractive Lens and Fresnel Lens in X-Ray Region," Jpn. J. Appl. Phys. **43**(10), 7311–7314 (2004).
24. F. J. Koch, C. Detlefs, T. J. Schröter, D. Kunka, A. Last, and J. Mohr , "Quantitative characterization of X-ray lenses from two fabrication techniques with grating interferometry," Opt. Exp. **24**(9), 9168–9177 (2010).
25. F. Seiboth, A. Schropp, M. Scholz, F. Wittwer, C. Rödel, M. Wünsche, T. Ullsperger, S. Nolte, J. Rahomäki, K. Parfeniukas, S. Giakoumidis, U. Vogt, U. Wagner, C. Rau, U. Boesenberg, J. Garrevoet, G. Falkenberg, E. C. Galtier, H. J. Lee, B. Nagler, and C. G. Schroer, "Perfect X-ray focusing via fitting corrective glasses to aberrated optics," Nat. Commun. **8**, 14623 (2017).
26. I. Mohacsi, I. Vartiainen, B. Rösner, M. Guizar-Sicairos, V. A. Guzenko, I. McNulty, R. Winarski, M. V. Holt, and C. David, "Interlaced zone plate optics for hard X-ray imaging in the 10 nm range," Sci. Rep. **7**, 43624 (2017).
27. H. C. Kang, G. B. Stephenson, C. Liu, R. Conley, A. T. Macrander, J. Maser, S. Bajt, and H. N. Chapman, "Synchrotron x-ray study of multilayers in Laue geometry," Proc. SPIE **5537**, (2004).
28. H. Yan, H. C. Kang, R. Conley, C. Liu, A. T. Macrander, G. B. Stephenson, and J. Maser, "Multilayer Laue Lens: A Path Toward One Nanometer X-Ray Focusing," X-Ray Optics and Instrumentation **2010**, 401854 (2010).
29. C. G. Schroer, "Focusing hard x-rays to nanometer dimensions using Fresnel zone plates," PRB **74**, 033405 (2006).
30. S. Bajt, H. N. Chapman, A. Aquila, and E. Gullikson, "High-efficiency x-ray gratings with asymmetric-cut multilayers," J. Opt. Soc. Am. A **29**(3), 216–230 (2012).
31. S. Bajt, M. Prasciolu, H. Fleckenstein, M. Domaracký, H. N. Chapman, A. J. Morgan, O. Yefanov, M. Messerschmidt, Y. Du, K. T. Murray, V. Mariani, M. Kuhn, S. Aplin, K. Pande, P. Villanueva-Perez, K. Stachnik, J. PJ Chen, A. Andrejczuk, A. Meents, A. Burkhardt, D. Pennicard, X. Huang, H. Yan, E. Nazaretski, Y. S. Chu, and C. E. Hamm, "X-ray focusing with efficient high-NA multilayer Laue lenses," Light Sci. Appl. **7**, 17162 (2018).
32. R. M. Bionta, K. M. Skulina, and J. Weinberg"Hard x-ray sputtered-sliced phase zone plates," Appl. Phys. Lett. **64**(8), 945–947 (1994).
33. T. Liese, V. Radisch, and H.-U. Krebs, "Fabrication of multilayer Laue lenses by combination of pulsed Laser deposition and focused ion beam," Rev. Sci. Instrum. **81**, 073710 (2010).
34. J. Kirz, "Phase zone plates for x rays and the extreme uv," J. Opt. Soc. Am. **64**(3), 301–309 (1974).
35. H. Yan, J. Maser, A. Macrander, Q. Shen, S. Vogt, G. B. Stephenson, and H. C. Kang, "Takagi-Taupin description of x-ray dynamical diffraction from diffractive optics with large numerical aperture," Phys. Rev. B **76**, 115438 (2007).
36. H. N. Chapman and A. V. Rode, "Geometric optics of arrays of reflective surfaces," Appl. Opt. **33**(13), 2419–2436 (1994).

37. R. Conley, C. Liu, J. Qian, C. M. Kewish, A. T. Macrander, H. Yan, H. C. Kang, J. Maser, and G. B. Stephenson, "Wedged multilayer Laue lens," Rev. Sci. Instrum. **79**, 053104 (2008).
38. A. J. Morgan, M. Prasciolu, A. Andrejczuk, J. Krzywinski, A. Meents, D. Pennicard, H. Graafsma, A. Barty, R. J. Bean, M. Barthelmess, D. Oberthuer, O. Yefanov, A. Aquila, H. N. Chapman, and S. Bajt, "High numerical aperture multilayer Laue lenses," Sci. Rep. **5**, 9892 (2015).
39. M. Prasciolu, A. F. G. Leontowich, J. Krzywinski, A. Andrejczuk, H. N. Chapman, and S. Bajt, "Fabrication of wedged multilayer Laue lenses," Opt. Mat. Express **5**(4), 228318 (2015).
40. E. Abbe, "Über einen neuen Beleuchtungsapparat am Mikroskop," Archiv für mikroskopische Anatomie **9**(1), 469–480 (1873).
41. Lord Rayleigh, "Investigations in Optics with special reference to the Spectroscope," Philos. Mag. **8**(49), 261–274 (1979).
42. M. Prasciolu, and S. Bajt, "On the Properties of WC/SiC Multilayers," Appl. Sci. **8**(4), 571 (2018).
43. S. Bajt, M. Prasciolu, A. J. Morgan, H. N. Chapman, J. Krzywinski, and A. Andrejczuk, "One Dimensional Focusing with High Numerical Aperture Multilayer Laue Lens," AIP Conf. Proc. **1696**, 020049 (2016).
44. A. Andrejczuk, J. Krzywinski, and S. Bajt, "Influence of imperfections in a wedged multilayer Laue lens for the focusing of X-rays investigated by beam propagation method," Nucl. Instr. Meth. Phys. Res. B **364**, 60–64 (2015).
45. K. Li, M. Wojcik, and C. Jacobsen, "Multislicing does it all- calculating the performance of nanofocusing X-ray optics," Opt. Exp. **25**, 1831–1846 (2017).
46. W. M. Haynes, *CRC Handbook of Chemistry and Physics, 92^{nd} ed.* (CRC, 2011), p. 4.96.
47. W. M. Haynes, *CRC Handbook of Chemistry and Physics, 92^{nd} ed.* (CRC, 2011), p. 4.88.
48. H. H. Hopkins , "The concept of partial coherence in optics," Proc. Royal Soc. A **208**(1093), 263–277 (1951).
49. P. S. Considine , "Effects of Coherence on Imaging Systems," J. Opt. Soc. Am. **56**(8), 1001–1009 (1966).
50. A. Papoulis, *Systems and Transforms with Applications in Optics, 1^{st} ed.* (McGraw-Hill, 1968).
51. B. Pan, K. Qian, H. Xie, and A. Asundi, "Two-dimensional digital image correlation for in-plane displacement and strain measurement: a review," Meas. Sci. Technol. **20**, 062001 (2009).
52. H. Yan, X. Huang, N. Bouet, J. Zhou, E. Nazaretski, and Y. S. Chu, "Achieving diffraction-limited nanometer-scale X-ray point focus with two crossed multilayer Laue lenses: alignment challenges," Opt. Exp. **25**(21), 25234–25242 (2017).
53. S. Niese, P. Krüger, A. Kubec, S. Braun, J. Patommel, C. G. Schroer, A. Leson, and E. Zschech, "Full-field X-ray microscopy with crossed partial multilayer Laue lenses," Opt. Exp. **1696**, 020049 (2016).
54. S. Vogt, H. N. Chapman, C. Jacobsen, and R. Medenwaldt , "Dark field X-ray microscopy: the effects of condenser/ detector aperture," Ultramicroscopy **87**, 25–44 (2001).
55. H. F. Poulsen, A. C. Jakobsen, H. Simons, S. R. Ahl, P. K. Cook, and C. Detlefs , "X-ray diffraction microscopy based on refractive optics," J. Appl. Cryst. **50**, 1441–1456 (2017).
56. J. Als-Nielsen, and D. McMorrow, *Elements of Modern X-ray Physics 2^{nd} ed.* (Wiley, 2011), p. 220.
57. J. W. Goodman, *Introduction to Fourier Optics* (McGraw-Hill, 1996).
58. A. Kubec, S. Braun, S. Niese, P. Krüger, J. Patommel, M. Hecker, A. Leson, and C. G. Schroer, "Ptychography with multilayer Laue lenses," J. Synchrotron Radiat. **21**, 1122–1127 (2014).
59. J. Vila-Comamala, A. Diaz, M. Guizar-Sicairos, A. Mantion, C. M. Kewish, A. Menzel, O. Bunk, and C. David, "Characterization of high-resolution diffractive X-ray optics by ptychographic coherent diffractive imaging," Opt. Exp. **19**(22), 21333–21344 (2011).
60. H. Yan, and Y. S. Chu, "Optimization of multilayer Laue lenses for a scanning X-ray microscope," J. Synchrotron Radiat. **20**, 89–97 (2013).
61. H. Yan, V. Rose, D. Shu, E. Lima, H. C. Kang, R. Conley, C. Liu, N. Jahedi, A. T. Macrander, G. B. Stephenson, M. Holt, Y. S. Chu, M. Lu, and J. Maser, "Two dimensional hard x-ray nanofocusing with crossed multilayer Laue lenses," Opt. Exp. **19**(16), 15069–15076 (2011).
62. X. Huang, W. Xu, E. Nazaretski, N. Bouet, J. Zhou, Y. S. Chu, and H. Yan , "Hard x-ray scanning imaging achieved with bonded multilayer Laue lenses," Opt. Exp. **25**(8), 8698–8704 (2017).
63. G. B. M. Vaughan, J. P. Wright, A. Bytchkov, M. Rossat, H. Gleyzolle, I. Snigireva, and A. Snigirev , "X-ray transfocators: focusing devices based on compound refractive lenses," J. Synchrotron Radiat. **18**, 125–133 (2011).
64. A. F. Pedersen, H. Simons, C. Detlefs, and H. F. Poulsen , "The fractional Fourier transform as a simulation tool for lens-based X-ray microscopy," J. Synchrotron Radiat. **25**, 717–728 (2018).
65. L. J. Allen and M. P. Oxley, "Phase retrieval from series of images obtained by defocus variation," Opt. Comm. **199**, 65–75 (2001).
66. H. F. Poulsen, P. K. Cook, H. Leemreize, A. F. Pedersen, C. Yildirim, M. Kutsal, A. C. Jakobsen, J. X. Trujillo, J. Ormstrup, and C. Detlefs , "Reciprocal space mapping and strain scanning using X-ray diffraction microscopy," J. Appl. Cryst. **51**, https://doi.org/10.1107/S1600576718011378 (2018).